Research article (Pre-Print) **Open Access**

Moisture-induced degradation of clay-bearing sandstone

You Wang* Falk K. Wittel †

January 28, 2026

Abstract

Clay-bearing sandstones used in the construction of historic monuments, churches, and castles are highly susceptible to contour scaling, which manifests as fractures parallel to the exposed facades. Repeated wetting–drying cycles accelerate material degradation through stiffness reduction and hygric deformation induced by swelling clays. This in turn alters the hygro-thermal (HT) properties of the stone. In this study, a scalar damage variable is employed within the framework of continuum damage mechanics to characterize the evolving damage state under the influence of moisture fields. The most critical climatic conditions leading to degradation are first identified through hygro-thermal simulations. Subsequently, a fully coupled hygro-thermo- mechanical (HTM) model is developed to account for both moisture transport and material degradation. The results demonstrate that contour scaling can occur solely due to moisture cycling, even in the absence of freezing or salt crystallization effects. Moreover, the predicted zones of damage localization and depths of water accumulation align well with on-site observations.

Keywords: clay-bearing sandstone; wetting-drying cycles; worst climatic conditions; HTM; damage localization

---

*ETH Zurich, Institute for Building Materials, HIF E 27, Laura-Hezner-Weg 7, CH-8093 Zurich, Switzerland; E-mail: you.wang@ifb.baug.ethz.ch; ORCID: 0009-0003-3305-6684

†ETH Zurich, Institute for Building Materials, HIF E 27, Laura-Hezner-Weg 7, CH-8093 Zurich, Switzerland; E-mail: fwittel@ethz.ch; ORCID: 0000-0001-8672-5464

1 Introduction

Clay-bearing sandstones are central to the built heritage as local building material for historic monuments, churches, and castles worldwide. One notable example is the Swiss grey molasse from which the Cathedral of Lausanne is built. These stones contain swelling clay minerals (e.g., smectites) that cause hygroexpansions with fluctuations in moisture, leading to internal stresses and gradual deterioration. On the exterior facade, the stone suffers from various weather-related degradation processes, of which contour scaling is the most severe. Contour scaling is a damage where a subsurface fracture develops a few centimeters beneath the stone surface, shown in Fig. 1a (documented in Refs. [39, 12, 20]). It initiates inside the stone and grows in a parallel plane to the exposed facade from the inside to the edges, independent of the material orientation and bedding of the sandstone block, before fragments detach. This damage evolution indicates that contour scaling is driven by the climatic conditions to which the material is exposed, rather than by inherent imperfections. Understanding and mitigating such degradation mechanisms is therefore crucial for preserving the built heritage constructed with these vulnerable sandstones. The growth of contour scaling from preexisting flaws due to nonuniform wetting patterns through the buckling mechanism during the wetting phase was investigated by Wangler et al. [37]. Additionally, Praticò [20] proposed damage mechanisms for crack growth, including freezing, salt crystallization, stress corrosion, and wetting-drying cycles, following Ref. [4]. All these explanations depend on a preexisting macroscopic defect. Generating scaling damage in an intact block of sandstone through accelerated weathering would strongly foster the development of countermeasures. However, to our knowledge, all attempts have been unsuccessful so far. Consequently, contour scaling cracks do not form spontaneously within the material; rather, they emerge from the coalescence of micro-damages that have previously locally deteriorated the material due to moisture variations.

The influence of swelling clays on the deterioration of sandstones has been widely recognized and extensively investigated for the last decades (see Refs. [30, 3, 36, 1, 11, 23, 34, 25]). Veniale et al. [30] showed that alternating moisture cycles with clay swelling and shrinkage result in degradation by intergranular micro-cracking within the sandstone that reduces strength and promotes disintegration. Swiss molasse is highly susceptible to deterioration, as clay minerals are present in the stone cement, which is intended to bind the grains together. The clays (smectites) swell even by two superimposing mechanisms [1]. This aligns with experimental observations by Siegesmund et al. [25], which indicate that swelling clay minerals induce high stresses

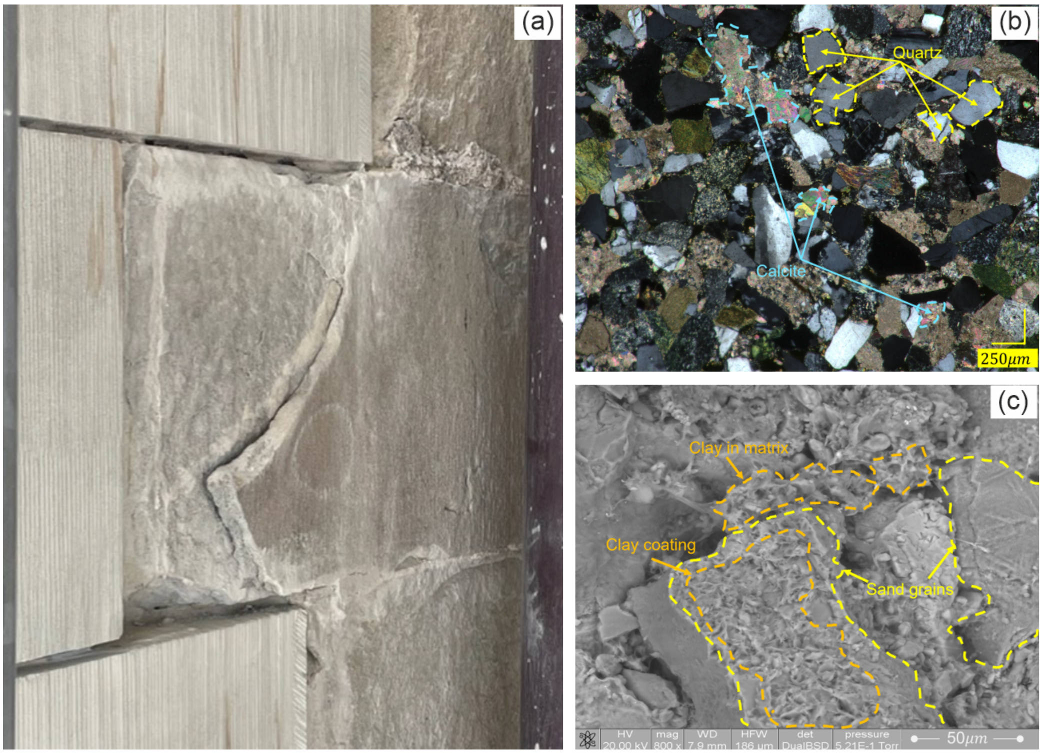

Figure 1: Contour scaling in a Villarlod molasse block used for restoration of the Cathedral of Lausanne (a), thin section fabric of Villarlod molasse under polarized light (b), and appearances of clay in an electron microscopy image (c).

and further degrade the rock fabric when they coat grains or fill micropores. Interestingly, damage was not observed for situations where swelling clays are located in macropores, since there is sufficient space for free expansion. A general and extensive review by Elert et al. [6] elaborated how cracks generate and progress from clay swelling and shrinkage in the clay-bearing sandstone.

In addition to experimental studies, efforts have recently been devoted to numerical modeling of moisture-related deterioration of rock containing swelling clay. From a grain scale perspective, Discrete Element (DE) Models were used to model different minerals (e.g., quartz and clay) by particles and investigate swelling-induced damages in rocks by expanding clay particles, as shown in Refs. [16, 13]. Zhang et al. [40] exploited Molecular Dynamics (MD) to simulate different phases in purple mudstone and associated clay swelling with the adsorption of water molecules in the interlayer space between clay-clay and silica-clay layers. At the continuum scale, damage constitutive models were proposed in Refs.[27, 38] for the clay-bearing sandstone and soft rock by incorporating a moisture-dependent damage variable. Nevertheless, these works do not capture the rock's structural response as it decays under changing moisture fields. To understand the role of clay-water interaction in stone deterioration from a macro scale, Wang and Yan [32] adopted a Finite-Discrete Element Method (FDEM) to consider moisture diffusion and crack propagation in hygro-responsive mudstone. The approach focused on macrocrack growth and neglected the initiation phase, which involves microcracking of the intact material. Moreover, the coupling between degradation and hygric properties of mudstone was neglected so far.

Despite the extensive body of research on water-clay interactions and their role in sandstone degradation, applying these insights to actual heritage structures requires greater attention. The first challenge is the hygro-thermo-mechanical (HTM) nature of the problem, in which the coupling among the different fields is of great importance. Contour scaling cannot be understood in isolation from the preceding material deterioration. The second challenge involves the different time scales of moisture and heat transport, as well as the variability in climatic conditions. In historic buildings, damage accumulates slowly, typically manifesting over periods ranging from decades to centuries. To experimentally reproduce contour scaling, accelerated weathering testing is a necessary prerequisite. Meaningful time-scaling of climatic influences on damage evolution can only be achieved through HTM simulations.

In this study, the evolution of moisture and material degradation is modeled in a fully coupled manner to investigate the effects of moisture cycles on damage evolution in Villarlod molasse, which is the preferred replacement stone for the Cathedral of Lausanne, after the closing of the grey molasse quarry in the 19^{th} century. DELPHIN 6, a hygro-thermal simulation program, is used to compute the moisture field in the presence of damage [7]. Simultaneously, the Finite Element (FE) solver ABAQUS 2024 calculates stress and strain fields, including the damage evolution, in the presence of moisture. Consequently, one needs to consider, on the one hand, the effects of moisture on the constitutive hygro-mechanical behavior, including the damage evolution law (Sec. 3.2), and on the other hand, the impact of damage on the hygro-thermal properties for moisture transport (Sec. 3.3). In the first step, we identify the worst-case scenario for climate change with respect to damage propagation, allowing us to focus on accelerated weather testing conditions (Sec. 5.1). These conditions are then periodically repeated to simulate the damage evolution in Villarlod molasse with the coupled framework (Sec. 5.2). We identify localized damage zones where contour scaling potentially initiates and describe its evolution. Finally, the effect of pressure distribution on the top of the sandstone is examined, revealing damage patterns in the stone under various constraints.

2 Problem statement and modelling idea

Although our results have general validity for clay-bearing sandstones, this study focuses on Villarlod molasse, as it serves as the replacement stone for the Cathedral of Lausanne. Hence, material parameters are specifically determined for Villarlod molasse, a soft, porous, glauconitic clay-bearing stone with a fine and grey appearance, characterized by thin bedding. The main phase of the sandstone is quartz, with around 50–60 % of the material by mass (see Refs. [25, 35]). Calcite is the cement that occurs as individual grains or bonds between quartz grains, and constitutes around 20–30 % of the stone by mass. These two components do not interact with moisture, but another crucial mineral in the Villarlod molasse, smectite, does. The fraction of smectite is around 5–6 % by mass according to Rietveld analysis [35]. For the sandstone, this results in observed swelling strains of up to $1.85\,\mathrm{mm\,m^{-1}}$ with water (Ref. [35]). Petrographic images of Villarlod molasse in Figs. 1b,c show the different phases of Villarlod molasse and the fineness of the stone. Since clay minerals are smaller in size than quartz and calcite grains, they are only visible via scanning electron microscopy (SEM) (see Fig. 1c). One finds clay that coats quartz grains, as well as in the intergranular matrix.

The goal of this study is to investigate the evolution of coupled moisture and damage fields in a wall composed of Villarlod molasse blocks, subject to wetting-drying cycles from the outer surface. One expects a cyclic damage progression, as damage modifies hygro-thermal properties, leading to moisture accumulation in zones with greater damage. This accumulation additionally softens and weakens these regions, while exerting higher residual stresses due to increased swelling, which further progresses damage. Using symmetry considerations, the problem can be reduced to a single sandstone half-block of a wall, shown in Fig. 2. It has a thickness of 60 cm and a height of 25 cm, carries the load from the upper structure, and has symmetry conditions below. Since contour scaling is growing in a plane parallel to the exposed facade, a plane-strain assumption can be applied for simplicity. Note that in reality, blocks also have a limited extension perpendicular to the plane (y-direction) and cannot transmit tensile stresses across edges. The upper surface takes the dead load of the entire wall above. However, a uniform pressure distribution would not reflect reality, as moisture fields result in material and shape changes. Due to symmetry, neither the upper nor the lower stone can deform in a way that they could penetrate the contact line. Additionally, contacting stones can locally detach from each other due to local shrinkage, forming a gap. Consequently, the load must be introduced via a rigid contact surface with the vertical force from the dead load being introduced at its reference point RP (see Fig. 2 ABAQUS model). For simplicity, a frictionless hard contact is applied between the contact surface and the block. The evolving damage field renders the originally one-dimensional problem with no vertical heat or moisture flux into a two-dimensional one (see Fig. 2 DELPHIN model). Due to symmetry considerations, there will be no flux across the upper surface and the symmetry line. Realistic climatic conditions typically involve multiple components, such as rain, sunlight, wind, and others. In the current study, we limit ourselves to simple wetting-drying cycles with rain for wetting and high temperature, as well as low relative humidity for drying. Furthermore, a constant indoor climate is assumed, with a temperature $T_{in} = 25\,^{\circ}\mathrm{C}$ and a relative humidity of $RH_{in} = 50\,\%$.

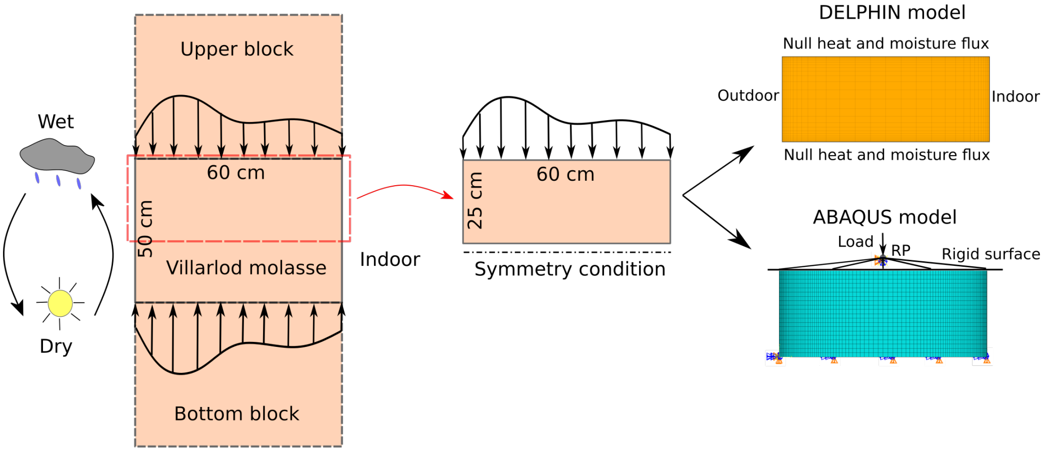

Figure 2: A representative block of the wall and model realizations in DELPHIN and ABAQUS (RP: reference point).

3 Model formulation

In this section, the physical foundation and respective model approaches used in this work for the transport of heat and mass in porous media, the moisture dependence of constitutive mechanical parameters, and the HTM coupling framework are bundled. The description of the hygro-thermal behavior (Sec. 3.1) focuses on the storage and transport of moisture (Secs. 3.1.1, 3.1.2), as well as transport of heat (Sec. 3.1.3), before the moisture dependence of the mechanical models is explained (Sec. 3.2). Finally, Sec. 3.3 illustrates how the coupling HTM framework is implemented. Note that a separate section is devoted to the identification of the required parameters (Sec. 4).

3.1 The hygro-thermal model

For calculating the fully coupled heat and moisture transport in porous sandstone, the widely used robust simulation software DELPHIN is applied (see Ref. [8]). Unlike simplified tools, it solves equations using efficient higher-order numerical methods, enabling accurate predictions of complex processes in porous building materials based on a comprehensive, thermodynamically sound physical model. The governing equations in this study are the mass and energy balances of moisture (liquid and vapor) and air, as presented in Ref. [18]. They can be written as

$$\frac{\partial(\rho_\mathrm{w}\theta_\mathrm{l}+\rho_\mathrm{v}\theta_\mathrm{g})}{\partial t} = -\frac{\partial[\rho_\mathrm{w}v_k^{m_\mathrm{l}}\theta_\mathrm{l}+(\rho_\mathrm{v}v_k^{m_\mathrm{g}}+j_{k,\mathrm{diff}}^{m_\mathrm{v}})\theta_\mathrm{g}]}{\partial x_k}, \tag{1a}$$

$$\frac{\partial\rho_\mathrm{a}\theta_\mathrm{g}}{\partial t} = -\frac{\partial[(\rho_\mathrm{a}v_k^{m_\mathrm{g}}-j_{k,\mathrm{diff}}^{m_\mathrm{v}})\theta_\mathrm{g}]}{\partial x_k}, \tag{1b}$$

$$\frac{\partial[\rho_\mathrm{m}u_\mathrm{m}+\rho_\mathrm{l}u_\mathrm{l}\theta_\mathrm{l}+(\rho_\mathrm{v}u_\mathrm{v}+\rho_\mathrm{a}u_\mathrm{a})\theta_\mathrm{g}]}{\partial t} = -\frac{\partial[\rho_\mathrm{l}u_\mathrm{l}v_k^{m_\mathrm{l}}\theta_\mathrm{l}+(\rho_\mathrm{v}u_\mathrm{v}+\rho_\mathrm{a}u_\mathrm{a})v_k^{m_\mathrm{g}}\theta_\mathrm{g}]}{\partial x_k} - \frac{\partial[j_{k,\mathrm{diff}}^{\mathrm{Q}}-(h_\mathrm{v}-h_\mathrm{a})j_{k,\mathrm{diff}}^{m_\mathrm{v}}\theta_\mathrm{g}]}{\partial x_k}, \tag{1c}$$

where variables ρ, m, θ, v, u, and h represent mass density, mass, volumetric fraction, phase velocity, energy density, and enthalpy, respectively. The liquid and gas phases are denoted by the subscripts l and g. Liquid water, vapor, and dry air are given by w, v, and a, respectively, and the subscript m stands for the skeleton of the porous material. In the equations, $j_{k,\mathrm{diff}}^{m_\mathrm{v}}$ denotes the mass flux of vapor, $j_{k,\mathrm{diff}}^{\mathrm{Q}}$ the heat flux via conduction, and k is the directional index. To solve the above governing equations, constitutive functions are required to describe the relation between the flux and the driving potential, which are written with the capillary pressure p_c as

$$\rho_\mathrm{w}v_k^{m_\mathrm{l}} = -K_\mathrm{l}(\frac{\partial p_\mathrm{c}}{\partial x_k}+\rho_\mathrm{w}g_k), \tag{2a}$$

$$j_{k,\mathrm{diff}}^{m_\mathrm{v}} = -K_\mathrm{v}\frac{\partial p_\mathrm{v}}{\partial x_k}, \tag{2b}$$

$$j_{k,\mathrm{diff}}^{\mathrm{Q}} = -\lambda\frac{\partial T}{\partial x_k}. \tag{2c}$$

The three conductivity coefficients K_l, K_v, and λ for liquid, vapor, and thermal conductivity are actually functions of the liquid content θ_l. Note that the capillary pressure is dependent on θ_l as well, which is known as the moisture storage function (MSF) (see Sec. 3.1.1).

The vapor pressure p_v is related to the relative humidity φ by $p_\mathrm{v} = \varphi p_{\mathrm{v,sat}}(T)$, where $p_{\mathrm{v,sat}}$ is the saturation vapor pressure which depends on temperature T. With the Kelvin equation

$$p_\mathrm{c} = \rho_\mathrm{l} R_\mathrm{v} T \ln \varphi = \rho_\mathrm{l} R_\mathrm{v} T \ln \frac{p_\mathrm{v}}{p_{\mathrm{v,sat}}}, \tag{3}$$

that uses the ideal gas constant of vapor R_v, and the MSF, one obtains the relation between p_v and θ_l. Substituting Eqs. 2 and 3 into Eqs. 1, the moisture content and temperature can be solved for, if the dependencies of K_l, K_v, λ, and p_c on θ_l are known.

3.1.1 Moisture storage $p_\mathrm{c}(\theta_\mathrm{l})$

The moisture storage behavior describes the amount of liquid a porous material can hold under a given moisture potential. The MSF is an important material property for material description, relating the state variable θ_l to a potential. As moisture potential, either the capillary pressure p_c or the relative humidity φ (related by the Kelvin Eq. 3 for pure water) can be regarded. The MSF thus makes the connection between the constitutive equations and the balance for equilibrium stages. Hence, the underlying characteristics of the porous material are reflected in suitable pore-space models. For sandstone, a model with p_c is chosen where the pore volume distribution is described with the aid of a weighted sum of Gauss distribution functions (see Ref. [24]):

$$\theta_\mathrm{l} = \sum_{i=1}^{N} \frac{\alpha_i}{\sqrt{2}} \left(1 + \mathrm{erf}\left(\frac{p_{\mathrm{clog},i} - p_\mathrm{clog}}{\sqrt{2} s_i}\right)\right), \tag{4}$$

where erf() is the Gauss error function, p_clog is the logarithmic capillary pressure, namely $\log(p_\mathrm{c})$, N represents the number of modalities of the pore volume distribution curve, and α_i, $p_{\mathrm{clog},i}$, s_i are parameters to be calibrated for each modality. It should be noted that even though hysteresis is quite common for moisture retention of most building materials [24], DELPHIN only requires a single moisture storage curve as input, which can still provide sufficient correspondence to experimental results in many practical cases [10].

3.1.2 Moisture transport

For accurate hygro-thermal simulations, it is essential to employ a suitable moisture transport model for both liquid water and vapor. In this work, a popular liquid transport function is employed, which is based on the bundle-of-tubes model, as presented in Refs. [2, 5, 24]. The basic assumption is that pores can be modeled as tubes with varying radii, following the material's pore-size distribution (PSD).

The liquid conductivity K_l is derived as

$$K_\mathrm{l}(\theta_\mathrm{l}) = \frac{\rho_\mathrm{l}\sigma_\mathrm{lg}^2}{2\eta_\mathrm{l}} \int_0^{\theta_\mathrm{l}} \frac{1}{p_\mathrm{c}^2(x)} \mathrm{d}x, \tag{5}$$

where ρ_l represents the density, θ_l its volume fraction, σ_lg is the surface tension at the liquid-air interface, and η_l the dynamic viscosity of the liquid water. Unfortunately, Eq. 5 overestimates K_l near full saturation, also called effective saturation θ_eff, as p_c becomes very small in this region. To avoid high integral values, Eq. 5 is only applied to liquid contents θ_l below capillary saturation θ_cap. For values above, a linear interpolation of the liquid conductivity is made from $K_\mathrm{l}(\theta_\mathrm{cap})$ up to $K_\mathrm{l}(\theta_\mathrm{eff})$ at effective saturation when all accessible pores are filled. The liquid conductivity function for the whole moisture range is given as

$$K_\mathrm{l}(\theta_\mathrm{l}) = \begin{cases} A_\mathrm{l} \int_0^{\theta_\mathrm{l}} \frac{1}{p_\mathrm{c}^2(x)} dx & \text{for } \theta_\mathrm{l} \leq \theta_\mathrm{cap} \\ \frac{K_\mathrm{l}(\theta_\mathrm{eff}) - K_\mathrm{l}(\theta_\mathrm{cap})}{\theta_\mathrm{eff} - \theta_\mathrm{cap}} (\theta_\mathrm{l} - \theta_\mathrm{cap}) + K_\mathrm{l}(\theta_\mathrm{cap}) & \text{for } \theta_\mathrm{cap} < \theta_\mathrm{l} \leq \theta_\mathrm{eff} \end{cases}, \tag{6}$$

with the substitution $A_\mathrm{l} = \rho_\mathrm{l}\sigma_\mathrm{lg}^2/2\eta_\mathrm{l}$. Note that A_l is treated as a parameter that needs to be calibrated rather than a constant since σ_lg and η_l are dependent on temperature and solute in the water.

The vapor conductivity function, however, is derived with the serial-parallel model presented in Refs. [9, 24]. It considers serial and parallel vapor transport as shown in Fig. 3.

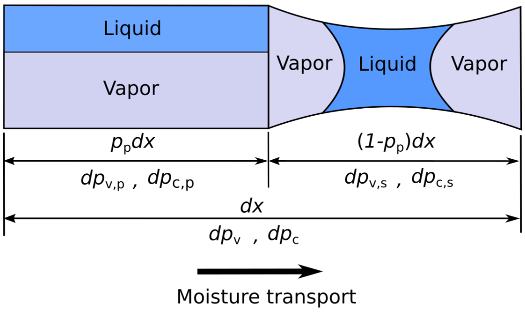

Figure 3: Serial-parallel model for moisture transport.

The total moisture flux density for the two transport types, serial and parallel, $\dot{m}_{\mathrm{tot}}^{\mathrm{ser}}$ and $\dot{m}_{tot}^{\mathrm{par}}$, is expressed by

$$\dot{m}_{\mathrm{tot}}^{\mathrm{ser}} = \dot{m}_{\mathrm{v}}^{\mathrm{ser}} = D_{\mathrm{v}}^{\mathrm{dry}} \frac{1}{1-\frac{\theta_{\mathrm{l}}}{\theta_{\mathrm{por}}}} \frac{1}{1-p_{\mathrm{p}}} \frac{\mathrm{d}p_{\mathrm{v,s}}}{\mathrm{d}x}, \tag{7a}$$

$$\dot{m}_{\mathrm{tot}}^{\mathrm{par}} = \dot{m}_{\mathrm{v}}^{\mathrm{par}} + \dot{m}_{\mathrm{l}}^{\mathrm{par}} = D_{\mathrm{v}}^{\mathrm{dry}} (1-\frac{\theta_{\mathrm{l}}}{\theta_{\mathrm{por}}}) \frac{1}{p_{\mathrm{p}}} \frac{\mathrm{d}p_{\mathrm{v,p}}}{\mathrm{d}x} + K_{\mathrm{l}}(\theta_{\mathrm{eff}}) \frac{1}{p_{\mathrm{p}}} \frac{\mathrm{d}p_{\mathrm{c,p}}}{\mathrm{d}x}, \tag{7b}$$

where $D_{\mathrm{v}}^{\mathrm{dry}}$ represents the vapor diffusion coefficient for the dry material, θ_{por} is the porosity, and $p_{\mathrm{v},k}$ and $p_{\mathrm{c},k}$ ($k = \mathrm{s}, \mathrm{p}$) are vapor and capillary pressure for serial and parallel transport. For continuity, $\dot{m}_{\mathrm{tot}}^{\mathrm{ser}} = \dot{m}_{tot}^{\mathrm{par}}$. Additionally, p_{p} is the proportion of the parallel transport that increases with the liquid content because more pores are filled with liquid water. Note that p_{p} slowly increases from zero for dry material, followed by rapid growth after a threshold liquid content, and finally converges to one near saturation. This behavior for p_{p} can be formulated in various ways, also with the aid of the function

$$p_{\mathrm{p}} = \frac{\gamma\left(1+10^{\frac{\theta_{\mathrm{trans}}}{\theta_{\mathrm{eff}}}}, 10^{\frac{\theta_{\mathrm{l}}}{\theta_{\mathrm{eff}}}}\right)}{\Gamma\left(1+10^{\frac{\theta_{\mathrm{trans}}}{\theta_{\mathrm{eff}}}}\right)}. \tag{8}$$

Here $\gamma(s,x)$ is the lower incomplete Gamma function expressed as $\gamma(s,x) = \int_0^x t^{s-1}e^{-t}dt$, and $\Gamma(s) = \int_0^\infty t^{s-1}e^{-t}dt$ is the Gamma function but with s being a real parameter. θ_{trans} represents the transition liquid content when liquid equates vapor conductivity. Eq. 8 is monotonically increasing with θ_{l}, as parallel transport becomes more dominant with the increase of the pore filling level, reaching values very close to one when $\theta_{\mathrm{l}} = \theta_{\mathrm{eff}}$. Additionally, two continuity conditions are obvious from Fig. 3, namely

$$\mathrm{d}p_{\mathrm{v}} = \mathrm{d}p_{\mathrm{v,s}} + \mathrm{d}p_{\mathrm{v,p}} \quad \text{and} \tag{9a}$$

$$\frac{\mathrm{d}p_{\mathrm{c,p}}}{\mathrm{d}x_p} = \frac{\mathrm{d}p_{\mathrm{c}}}{\mathrm{d}x}. \tag{9b}$$

Inserting those into Eqs. 7, one gets the total moisture flux density $\dot{m}_{\mathrm{tot}}$ as

$$\dot{m}_{\mathrm{tot}} = \dot{m}_{\mathrm{tot}}^{\mathrm{ser}} = D_{\mathrm{v}}(\theta_{\mathrm{l}}) \frac{\mathrm{d}p_{\mathrm{v}}}{\mathrm{d}x} + K_{\mathrm{l}}(\theta_{\mathrm{l}}) \frac{\mathrm{d}p_{\mathrm{c}}}{\mathrm{d}x}, \tag{10}$$

where $K_{\mathrm{l}}(\theta_{\mathrm{l}})$ is the liquid conductivity that will not be further considered here, mainly because $K_{\mathrm{l}}(\theta_{\mathrm{l}})$ is already taken care of via the bundle-of-tubes model as shown in Eq. 6. Furthermore, $D_{\mathrm{v}}(\theta_{\mathrm{l}})$ is the vapor diffusivity expressed by the dry vapor diffusion coefficient and the vapor scaling function $f_{\mathrm{v}}(\theta_{\mathrm{l}})$ written as

$$D_{\mathrm{v}}(\theta_{\mathrm{l}}) = D_{\mathrm{v}}^{\mathrm{dry}} f_{\mathrm{v}}(\theta_{\mathrm{l}}), \tag{11}$$

with

$$f_{\mathrm{v}}(\theta_{\mathrm{l}})=\frac{1-\frac{\theta_{\mathrm{l}}}{\theta_{\mathrm{eff}}}}{p_{\mathrm{p}}+\left(1-\frac{\theta_{\mathrm{l}}}{\theta_{\mathrm{eff}}}\right)^{2}(1-p_{\mathrm{p}})}. \tag{12}$$

Using the ideal gas equation, one can derive that vapor conductivity is simply the vapor diffusivity rescaled by the reciprocal thermodynamic factor $R_{\mathrm{v}}T$, namely

$$K_{\mathrm{v}}(\theta_{\mathrm{l}})=\frac{D_{\mathrm{v}}(\theta_{\mathrm{l}})}{R_{\mathrm{v}}T}, \tag{13}$$

with the gas constant of vapor R_{v}=462 J kg^{-1} K^{-1} and temperature T. Typically, dry cup tests are performed to measure $D_{\mathrm{v}}^{\mathrm{dry}}$. Unfortunately, the samples are not totally dry but have a small liquid content θ_{dry}. Therefore, the ultimate expression of K_{v} is given by combining Eqs. 11 and 13 with the corrected vapor diffusion coefficient $D_{\mathrm{v}}(\theta_{\mathrm{dry}}) = D_{\mathrm{v,air}}/\mu_{\mathrm{dry}}$ and $D_{\mathrm{v}}^{\mathrm{dry}} = D_{\mathrm{v}}(\theta_{\mathrm{dry}})/f_{\mathrm{v}}(\theta_{\mathrm{dry}}) = D_{\mathrm{v,air}}/(\mu_{\mathrm{dry}}f_{\mathrm{v}}(\theta_{\mathrm{dry}}))$ as

$$K_{\mathrm{v}}=\frac{D_{\mathrm{v,air}}}{\mu_{\mathrm{dry}}R_{\mathrm{v}}T}\frac{f_{\mathrm{v}}(\theta_{\mathrm{l}})}{f_{\mathrm{v}}(\theta_{\mathrm{dry}})}, \quad \text{for} \quad \theta_{\mathrm{l}}\leq\theta_{\mathrm{por}}. \tag{14}$$

Here μ_{dry} denotes the vapor diffusion resistance from the dry cup test, and $D_{\mathrm{v,air}}$ represents the vapor diffusivity in the air that is related to the temperature T and ambient pressure p by the equation for the vapor diffusivity in air (see Ref. [41]), namely

$$D_{\mathrm{v,air}}=2.306\times10^{-5}\cdot\frac{p_0}{p}\cdot\left(\frac{T}{T_0}\right)^{1.81}. \tag{15}$$

p_0 is the reference atmospheric pressure equal to 1.01×10^{5} Pa and T_0 =273.15 K. With $T = 293.15$ K and $p = p_0$, $D_{\mathrm{v,air}}$ is taken as 2.62×10^{-5} m^{2} s^{-1} throughout this study.

To summarize: the liquid conductivity function in Eq. 6 has 4 parameters to be calibrated, namely A_{l}, θ_{cap}, θ_{eff}, and $K_{\mathrm{l}}(\theta_{\mathrm{eff}})$, just like the vapor conductivity function in Eq. 14 where the required 4 parameters for calibration are μ_{dry}, θ_{dry}, θ_{por}, and θ_{trans}.

3.1.3 Heat transport

Since the drying rate of a material is influenced by temperature, its thermal properties are important. In sandstone, diffusive heat transfer is dominant, which is characterized by the thermal conductivity λ as written in Eq. 2c. Generally, thermal conductivity increases with increasing moisture content.

DELPHIN utilizes a simple linear dependence of λ on the liquid content with an assumed slope of $0.56\,\mathrm{W\,m^{-1}\,K^{-1}}$ (see Ref. [31]), namely

$$\lambda(\theta_\mathrm{l}) = \lambda_\mathrm{dry} + 0.56\theta_\mathrm{l}. \tag{16}$$

In Eq. 16, λ_dry is the thermal conductivity of dry Villarlod molasse.

3.2 Effect of moisture on the mechanical model

Moisture acts on Villarlod molasse in various ways through interactions between clay and water. As moisture increases, the stone becomes weaker, swells, and softens. However, the increase in compliance can be attributed not only to the softening of the clay phase but also to the progression of dispersed damage. In this work, we consider damage by a scalar damage variable D ranging from 0 to 1 in an isotropic fashion, following Ref. [17]. The Young's modulus of the sandstone in the presence of damage and moisture is reduced as

$$E(D,\theta_\mathrm{l}) = (1-D)E_0(\theta_\mathrm{l}), \tag{17}$$

where $E_0(\theta_\mathrm{l})$ is the moisture-dependent Young's modulus of the intact sandstone. Since the material block in this study allows for the reduction of the stress state to a plane strain condition, only two normal and one shear components need to be considered for stress $\boldsymbol{\sigma}$ and strain $\boldsymbol{\epsilon}$, reducing the secant stiffness matrix $\boldsymbol{S}$ to

$$\boldsymbol{S} = \begin{pmatrix} \lambda_\mathrm{l}+2\mu_\mathrm{l} & \lambda_\mathrm{l} & 0 \\ \lambda_\mathrm{l} & \lambda_\mathrm{l}+2\mu_\mathrm{l} & 0 \\ 0 & 0 & \mu_\mathrm{l} \end{pmatrix}. \tag{18}$$

λ_l and μ_l are the Lamé constants and expressed with the Poisson's ratio ν as

$$\lambda_\mathrm{l} = \frac{E(D,\theta_\mathrm{l})\nu}{(1+\nu)(1-2\nu)} \quad \text{and} \quad \mu_\mathrm{l} = \frac{E(D,\theta_\mathrm{l})}{2(1+\nu)}. \tag{19}$$

Due to the brittleness of sandstone, plastic deformations can be neglected. Consequently, the total strain $\boldsymbol{\epsilon}_\mathrm{tot}$ is only composed of elastic $\boldsymbol{\epsilon}_\mathrm{ela}$ and hygric strain $\boldsymbol{\epsilon}_\mathrm{hyg}$, namely

$$\boldsymbol{\epsilon}_\mathrm{tot} = \boldsymbol{\epsilon}_\mathrm{ela} + \boldsymbol{\epsilon}_\mathrm{hyg}. \tag{20}$$

$\boldsymbol{\epsilon}_\mathrm{hyg}$ is calculated from the moisture and written in vectorial form as

$$\boldsymbol{\epsilon}_\mathrm{hyg} = \epsilon_\mathrm{hyg}(\theta_\mathrm{l})(1,1,0)^T, \tag{21}$$

where $\epsilon_\mathrm{hyg}(\theta_\mathrm{l})$ is the magnitude of hygric strain at a given moisture content. Note that hygric deformation will affect only the normal strain components.

The stress is then calculated from the elastic strain using Hooke's law with the undamaged secant stiffness matrix $\boldsymbol{S}_0$ as

$$\boldsymbol{\sigma} = \boldsymbol{S} : \boldsymbol{\epsilon}_{\mathrm{ela}} = (1-D)\boldsymbol{S}_0 : (\boldsymbol{\epsilon}_{\mathrm{tot}} - \boldsymbol{\epsilon}_{\mathrm{hyg}}). \tag{22}$$

The damage evolution law in this study prescribes the damage driven by the deformation with respect to the maximum principal strain in history, $\epsilon_{\max}$, as

$$D(\epsilon_{\max}, \theta_{\mathrm{l}}) = \begin{cases} \frac{g(\epsilon_{\mathrm{f}}(\theta_{\mathrm{l}}))(1-\exp(-\beta\epsilon_{\max}))}{(g(\epsilon_{\mathrm{f}}(\theta_{\mathrm{l}}))-1)(1+g(\epsilon_{\mathrm{f}}(\theta_{\mathrm{l}}))\exp(-\beta\epsilon_{\max}))} & \text{for } D \leq 0.4, \epsilon_{\max} \geq 0, \\ 0.4 & \text{for } D > 0.4, \epsilon_{\max} \geq 0 \\ 0 & \text{for } \epsilon_{\max} < 0. \end{cases}, \tag{23}$$

In Eq. 23 β is a function parameter, ϵ_{f} is the strain at full damage of the sandstone $(D = 1)$ that depends on the moisture content θ_{l} as

$$\epsilon_{\mathrm{f}} = 15\frac{\sigma_{\mathrm{t}}(\theta_{\mathrm{l}})}{E_0(\theta_{\mathrm{l}})}, \tag{24}$$

and $g(\epsilon_{\mathrm{f}}(\theta_{\mathrm{l}})) = \exp(0.5\beta\epsilon_{\mathrm{f}}(\theta_{\mathrm{l}}))$. The damage evolution law in Eq. 23 is plotted in Fig. 4 for different values of β.

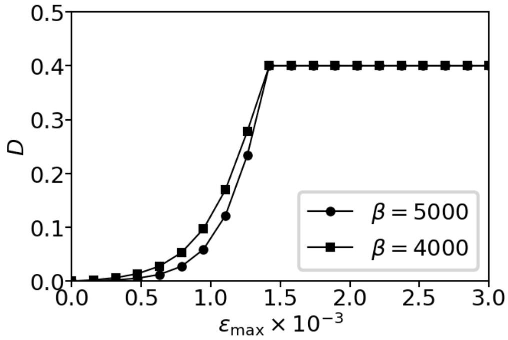

Figure 4: Damage evolution laws for $\epsilon_{\mathrm{f}} = 3 \times 10^{-3}$ and different β.

$\sigma_{\mathrm{t}}(\theta_{\mathrm{l}})$ in Eq. 24 is the tensile strength of Villarlod molasse, which decreases with increasing moisture content. This introduces the moisture dependency of the damage variable D together with $E_0(\theta_{\mathrm{l}})$. The coefficient 15 is chosen because the tensile strength only characterizes the initiation of damage instead of the fully damaged state. One can simply check the limiting cases $D = 0$ for $\epsilon_{\max} = 0$ and $D = 1$ when $\epsilon_{\max} = \epsilon_{\mathrm{f}}$. The damage variable is limited to a threshold value of 0.4, since such high values would mean fracture formation in sandstone [14]. Damage variables beyond 0.4 further reduce the stiffness but also lead to numerical difficulties.

The tangent stiffness, defined as the derivative of stress with regard to strain, is required by the FEM solver. It can be calculated from Eq. 22 as

$$\frac{\partial \boldsymbol{\sigma}}{\partial \boldsymbol{\epsilon}_{\text{tot}}} = (1-D)\boldsymbol{S}_0 - (\boldsymbol{S}_0 : (\boldsymbol{\epsilon}_{\text{tot}} - \boldsymbol{\epsilon}_{\text{hyg}}))\,(\frac{\partial D}{\partial \epsilon_{\text{max}}}\frac{\partial \epsilon_{\text{max}}}{\partial \boldsymbol{\epsilon}_{\text{tot}}}). \tag{25}$$

Note that Eq. 25 results in an asymmetric stiffness matrix that leads to poor numerical convergence. Moreover, upon unloading, the damage variable does not evolve, meaning that the second term on the right-hand side of Eq. 25 vanishes abruptly at stress reversion. This non-smooth transition of the damage variable leads to additional convergence issues that are addressed by the viscous regularization technique, which smoothens the evolution of the damage (see Ref. [15]). The regularized damage variable is updated by

$$D_{\text{vis}}^{n+1} = \frac{\eta}{\eta + \Delta t} D_{\text{vis}}^{n} + \frac{\Delta t}{\eta + \Delta t} D^{n+1}, \tag{26}$$

where D_{vis} is the damage variable after regularization, η is the viscosity parameter that controls how fast D_{vis} approaches D, the subscript n is the time increment number, and Δt is the time increment size. Thus, the damage variable D that occurs in Eqs. (22) and (25) are replaced by D_{vis}.

3.3 HTM framework

The hygro-thermal and mechanical models are intrinsically coupled, as moisture variations influence the progression of damage. At the same time, the resulting material degradation alters the porosity and pore-size distribution of the Villarlod molasse, thereby modifying its hygrothermal behavior. Emerging microcracks will modify the PSD by introducing a progressively more pronounced secondary peak associated with smaller pores, corresponding to open microcracks. The PSD of undamaged Villarlod molasse, shown in Fig. 5, exhibits a single peak around 10 µm, whereas Sander sandstone displays two characteristic peaks. Sander sandstone is therefore considered representative of the fully damaged state of Villarlod molasse. Intermediate damage states, characterized by values of the damage variables between 0 and 1, are assumed to have PSDs that can be approximated by linear interpolation between the two reference PSDs.

To efficiently couple the HTM model, 100 material datasets are precomputed for damage variables spanning the interval $[0, 1]$. During model execution, each material update in the hygro-thermal (HT) simulation is performed through a simple dictionary lookup to identify the dataset corresponding to the nearest damage state.

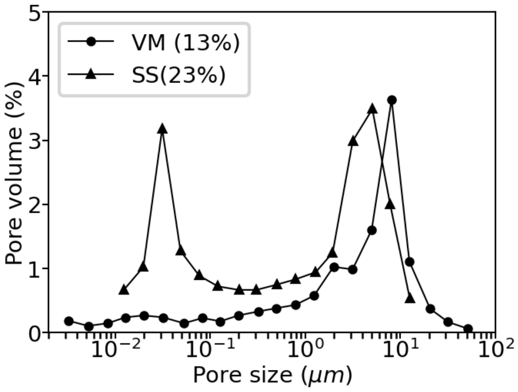

Figure 5: PSD of Villarlod molasse (VM) from Ref. [25] and Sander sandstone (SS) from Ref. [26].

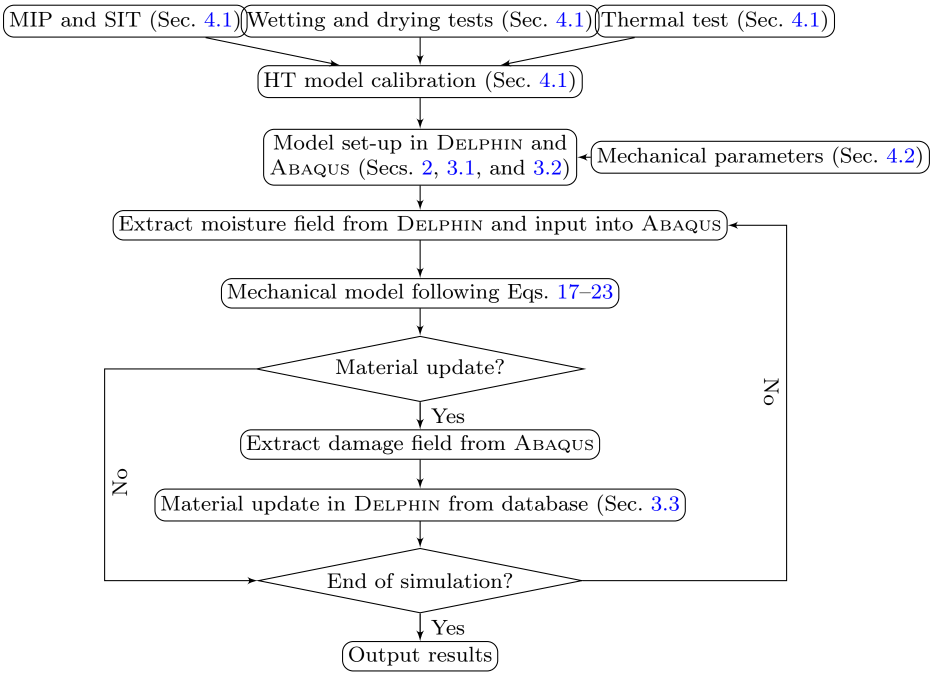

Figure 6: Workflow of the coupling model framework.

The entire block is discretized into small patches within which the material is homogeneous and updated collectively. This approach introduces material heterogeneity by accounting for spatial variations in the local damage state, resulting in more realistic and stable simulations. To limit computational cost, the material properties are not updated at every time increment in ABAQUS but at predefined intervals, namely 1 h. In general, the HTM framework operates as follows:

Step 1. Retrieve the current damage field over the domain when a material update is required;

Step 2. Reassign the material properties in all patches and compute the updated moisture profile using the hygro-thermal (HT) model within Delphin;

Step 3. Evaluate strains, stresses, and related quantities in Abaqus based on the current moisture profile;

Step 4. Extract the updated damage variables. If another material update is required, return to Step 1; otherwise, repeat Step 3 for the next time increment in Abaqus.

The detailed workflow of the coupling framework is displayed by the flowchart in Fig. 6.

Because HT and HTM models use different solvers, the meshes used differ (see Fig. 7). Material sections are assigned to patches in Delphin, which are defined in the FEM mesh by grouping 3 elements in a row and 2 elements in a column, as shown in Fig. 7. Each element in Delphin is then assigned to the patch if its center falls within the patch. The moisture profile obtained from Delphin is mapped to the integration points of the elements in Abaqus using linear interpolation. Finally, the resulting damage from the HTM simulation is averaged by taking the mean value of all damage states inside each patch for the next material update and HT iteration.

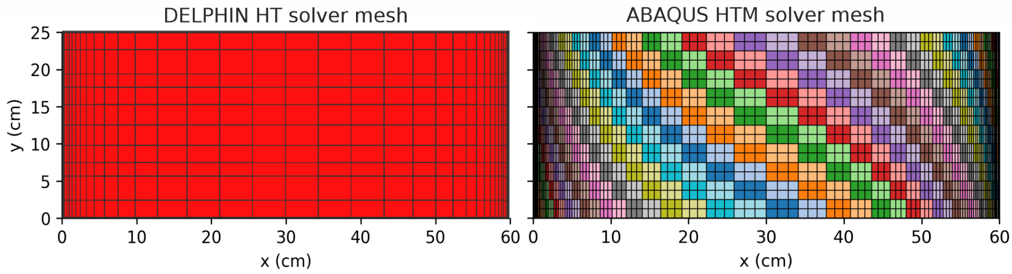

Figure 7: Mesh for the HT simulation with Delphin (left) and the damage calculation with Abaqus. Colors distinguish regions for individual material assignments.

4 Parameter identification

The HTM model, like any numerical framework, relies on multiple parameters (described in Sec. 3) that must be obtained either from dedicated material experiments or from literature sources. Since the overall framework involves two coupled models, the experiments for parameter identification for the hygro-thermal (HT) model are summarized first (Sec. 4.1), followed by those of the mechanical model (Sec. 4.2).

4.1 HT model parameters

The moisture storage curve parameters (i.e., α_i, $p_{\mathrm{clog},i}$, and s_i in Eq. 4) are calibrated on data of **mercury intrusion porosimetry** (MIP) published in Ref. [25] as well as on sorption isotherm lab tests, performed for this study. Based on the calibrated moisture storage curve, the moisture transport properties (i.e., A_{l}, θ_{cap}, θ_{eff}, $K_{\mathrm{l}}(\theta_{\mathrm{eff}})$, μ_{dry}, θ_{dry}, θ_{por}, and θ_{trans} in Eqs. 6 and 14) are identified. For this purpose, two moisture-transport lab experiments are conducted on sandstone blocks: the drying and the water-uptake tests. The transport parameters are then determined inversely using a Bayesian optimization procedure to achieve agreement between simulations and their respective test results. In the last experiment, the dry thermal conductivity λ_{dry} is directly measured by a thermal conductivity meter.

The PSD obtained from MIP can be translated into the relation between capillary pressure and moisture content via the Laplace equation:

$$p_{\mathrm{c}} = \frac{2\sigma_{\mathrm{lg}} \cos\theta}{r}. \tag{27}$$

σ_{lg} denotes the surface tension between air and water, θ represents the contact angle which is taken as zero for mercury in this study (wetting), and r is the pore radius. However, using MIP to obtain the moisture storage curve is valid only at low capillary pressure, namely, high liquid content, as the MIP test mimics the stone's desaturation process. To obtain the full range of the moisture storage behavior, **static gravimetric sorption tests** were performed at a constant temperature of 23 °C to obtain the sorption isotherm. Different salt solutions were used to create relative humidity levels ranging from 90 % to 20 % in a desiccator, with three $4 \times 4 \times 4$ cm large samples being tested. The samples were first saturated and then equilibrated at a single relative humidity to determine the corresponding liquid content by mass before being moved to the next lower relative humidity. The calibrated moisture storage curve is plotted in Fig. 8. For consistency, an artificial point with a moisture content of 0 is added at a capillary pressure of 10^{12} Pa where the moisture storage curve ends. Note that an even better fit could be obtained by increasing the number of modalities of the pore volume distribution curve N from Eq. 4. However, $N = 8$ is used in this study, as excessive modes of the MSF would lead to numerical problems during later calibration of the moisture transport functions.

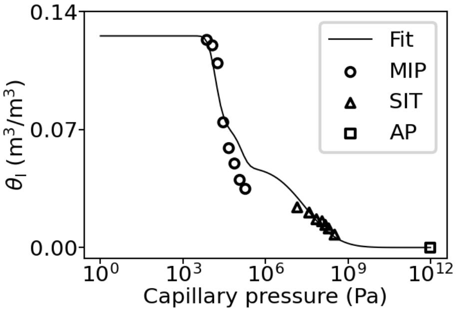

Figure 8: Calibrated moisture storage curve with MIP, sorption isotherm test (SIT), and the artificial point (AP).

For the water uptake and drying tests, three samples of identical dimensions of (4 × 4 × 4 cm) were used. In the **water uptake test**, each sample was suspended from a balance (METTLER PM 4000, precision as 0.01 g) with its bottom surface in full contact with deionized water, as illustrated in Fig. 9(a). The balance continuously recorded the sample mass until equilibrium was reached, from which the liquid content was calculated. For Villarlod molasse, equilibrium was typically attained within 2–3 h.

In contrast, the **drying test** took substantially longer, as vapor diffusion proceeds much more slowly than capillary absorption. For this test, the samples were first fully saturated and then placed in a climate chamber maintained at 25 °C and 35 % relative humidity. Equilibrium conditions were reached approximately after two weeks.

Subsequently, the drying and water-uptake tests are simulated in DELPHIN to calibrate the moisture-transport parameters using the Bayesian optimization technique. The loss function for optimization is formulated as the error between simulations and both experiments. Since the two tests have quite different scales, the numerical and experimental results are normalized to the maximum and minimum values from the lab tests, so that they fall within the interval $[0, 1]$. The calibration result is shown in Fig. 10, where the test results are the average of the three samples used in the experiments.

The **dry thermal conductivity**, λ_{dry} in Eq. 16, was determined using a thermal conductivity meter (Kemtherm QTM-D3, precision as 5 % of the reference value) on a specimen with dimensions of $18 \times 25.5 \times 15$ cm, as shown in Fig. 9(b). The measured value of λ_{dry} is $1.73\,\mathrm{W\,m^{-1}\,K^{-1}}$.

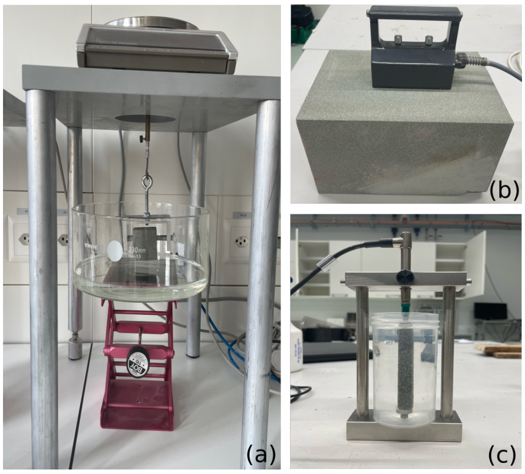

Figure 9: Experimental setups: (a) Water uptake test; (b) Thermal test; (c) Longitudinal swelling test.

The calibrated hygro-thermal parameters of Villarlod molasse are summarized in Table 1 along with other model parameters and their reference to literature.

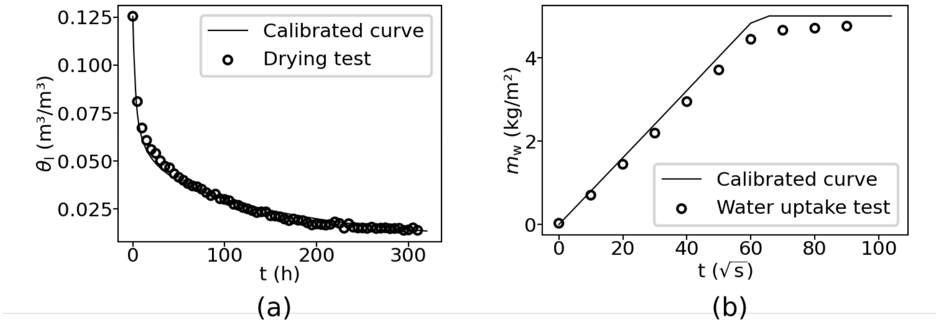

Figure 10: Comparison between experimental data and numerical results obtained with calibrated material behavior: (a) Drying test; (b) Water uptake test (m_{w}: Cumulative water uptake per unit area).

4.2 Mechanical model parameters

The previously described mechanical model of the HTM framework (see Sec. 3.2), requires additional parameters to be determined, such as the moisture dependence of the Young's modulus $E_0(\theta_{\mathrm{l}})$, the Poisson's ratio ν, the hygro-expansion behavior $\epsilon_{\mathrm{hyg}}(\theta_{\mathrm{l}})$, and the damage evolution law formulated in Eq. 23.

Table 1: HT model parameters and constants.

Quantities	**Value**	**Source**
Identified model parameters		
Coefficient in $K_l(\theta_l)$	$A_l = 3.39\,\mathrm{Pa^2\,s}$	Calibration
Liquid conductivity at θ_{eff}	$K_l(\theta_{\mathrm{eff}}) = 2.38 \times 10^{-9}\,\mathrm{s}$	Calibration
Porosity	$\theta_{\mathrm{por}} = 0.179$	Calibration
liquid content in dry cup test	$\theta_{\mathrm{dry}} = 0.002\,\mathrm{m^3\,m^{-3}}$	Calibration
Vapor resistance from dry cup test	$\mu_{\mathrm{dry}} = 11.18$	Calibration
Effective saturation	$\theta_{\mathrm{eff}} = 0.125\,\mathrm{m^3\,m^{-3}}$	Calibration
Transition liquid content	$\theta_{\mathrm{trans}} = 0.048\,\mathrm{m^3\,m^{-3}}$	Calibration
MSF	Fig. 8	Calibration
Thermal conductivity at dry state	$\lambda_{\mathrm{dry}} = 1.73\,\mathrm{W\,m^{-1}\,K^{-1}}$	Measurement
Model parameters from literature		
Vapor diffusivity of air under 20°C	$D_{\mathrm{v,air}} = 2.62 \times 10^{-6}\,\mathrm{m^2\,s^{-1}}$	Ref.[41]
Ideal gas constant of vapor	$R_{\mathrm{v}} = 462\,\mathrm{J\,kg^{-1}\,K^{-1}}$	Ref.[41]
Reference gas pressure	$p_0 = 1.01 \times 10^5\,\mathrm{Pa}$	Ref.[41]

According to Ref. [29], the Young's moduli of Villarlod molasse under relative humidities of 0, 33 %, 67 %, and 97 % are measured as 8.43 GPa, 4.46 GPa, 4.39 GPa, and 2.61 GPa, respectively. The moisture content corresponding to each relative humidity is obtained from Eq. 3 and the moisture storage curve in Fig. 8. The behavior for $E_0(\theta_l)$ can be described by an exponential function of the type

$$E_0(\theta_l) = A_{\mathrm{E}} e^{-B_{\mathrm{E}}\theta_l} + C_{\mathrm{E}}, \tag{28}$$

with the fitting parameters A_{E}, B_{E}, and C_{E}. The best fit is confronted with the experimental data in Fig. 11a.

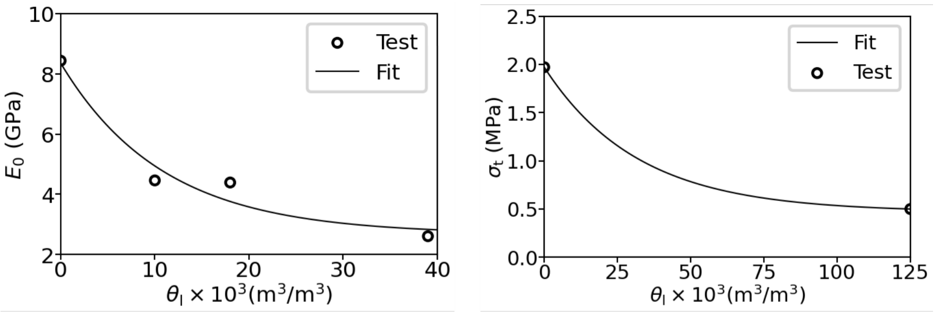

(a) (b)

Figure 11: Variation of Young's modulus (a) and tensile strength (b) with moisture content.

For the hygric expansion curve, a longitudinal swelling experiment is conducted in this study. The Villarlod molasse sample has an initial length of

80.9 mm and is immersed into the water, as shown in Fig. 9(c). A Linear Variable Differential Transformer (LVDT sensor) is placed on the top to measure the swelling deformation, plotted in Fig. 12a.

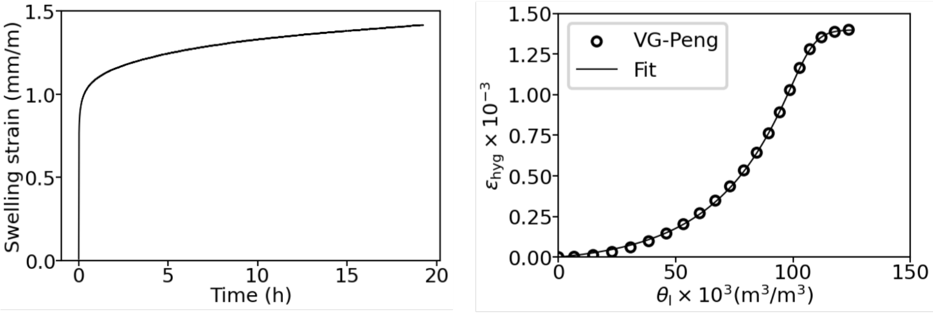

(a) (b)

Figure 12: Results of the longitudinal swelling test in the lab and hygric expansion curve of swelling clay from literature: (a) Evolution of swelling strain with time in the swelling test; (b) Fitted hygric expansion curve according to Ref. [22].

According to Ref. [22], the variation of swelling clay's void ratio with the moisture content can be described with the VG-Peng model proposed by Peng and Horn [19] that is expressed as

$$e(\zeta) = e_{\text{r}} + (e_{\text{s}} - e_{\text{r}})[1 + (\kappa\zeta)^{-p}]^{-q}, \quad \text{for} \quad 0 \le \zeta \le \zeta_{\text{s}}, \tag{29}$$

where e is the void ratio defined by the pore volume divided by the solid skeleton volume, ζ is the moisture ratio defined by the water volume divided by the solid skeleton volume, ζ_{s} is the saturated moisture ratio, e_{r} and e_{s} are residual and saturated void ratios, respectively, and κ, p, and q are fitting parameters. Actually, the change in void ratio with moisture content can be translated into volumetric strain and, in turn, into strain in one dimension. Taking the calibrated parameters for Eq. 29 from Ref. [22], the hygric expansion curve $\epsilon_{\text{hyg}}(\theta_{\text{l}})$ is fitted with a Richards function that is cast as

$$\epsilon_{\text{hyg}}(\theta_{\text{l}}) = A_\epsilon \left(1 + B_\epsilon \exp\left\{-C_\epsilon\left(\frac{\theta_{\text{l}}}{\theta_{\text{eff}}} - D_\epsilon\right)\right\}\right)^{-\frac{1}{F_\epsilon}}, \tag{30}$$

where A_ϵ, B_ϵ, C_ϵ, D_ϵ, and F_ϵ are fitting parameters. The fitted curve is shown in Fig. 12b, which is scaled in terms of the swelling strain measurement at saturation in Fig. 12a.

The tensile strength of the sandstone in Eq. 24 is also assumed to vary exponentially with the moisture content as

$$\sigma_{\text{t}}(\theta_{\text{l}}) = A_{\sigma_{\text{t}}} \exp\{-B_{\sigma_{\text{t}}}\theta_{\text{l}}\} + C_{\sigma_{\text{t}}}, \tag{31}$$

where A_{σ_t}, B_{σ_t}, and C_{σ_t} are functional parameters. According to Ref. [28], the tensile strengths under dry and saturated states are 1.97 MPa and 0.50 MPa, respectively. Eq. 31 is then fitted and plotted in Fig. 11b. Unfortunately, only two points are available here for fitting, and thus the limit of the exponential function in Eq. 31 is assumed to be just a little bit lower than the value at saturation in order to determine the three functional parameters. The strain at full damage, ϵ_f, can then be estimated with Eq. 24.

The last missing parameter of the mechanical model is the contact stiffness K_ct between the sandstone and the rigid plate on the top of the block shown in Fig. 2, which should depend on the stiffness of the deformable body, namely the sandstone. In this study, it is calculated with the Young's modulus of dry Villarlod molasse and the size of elements in contact with the rigid plate, denoted by h_c. The model in ABAQUS is discretized equally into twenty 8-node plane strain elements (CPE8) in the vertical direction, and thus $h_\mathrm{c} = 0.0125\,\mathrm{m}$ (see Fig. 7). All the parameters used in the mechanical model are summarized in Table 2.

Table 2: Parameters of the moisture-dependent mechanical model.

Parameter	**Value**	**Fitting source**
	Decay function of Young's modulus	
A_E	5.67 GPa	Ref. [29]
B_E	92	
C_E	2.68 GPa	
	Swelling curve	
A_ϵ	1.44×10^{-3}	Ref. [22]
B_ϵ	1.65	
C_ϵ	32.41	
D_ϵ	0.84	
F_ϵ	7.88	
	Decay function of tensile strength	
A_{σ_t}	1.50 MPa	Ref. [28]
B_{σ_t}	30	
C_{σ_t}	0.47 MPa	
	Other parameters	
Poisson's ratio ν	0.3	Ref. [28]
Damage parameter β	5000, 4000	Hypothesis
Viscosity parameter η	0.5	Hypothesis
Contact stiffness K_ct	$640\,\mathrm{GPa\,m^{-1}}$	$\frac{E_0(0)}{h_\mathrm{c}}$

5 Results and discussion

In a first step, pure HT simulations are conducted to identify the worst climatic conditions that have the potential to cause the greatest damage within the structure (Section 5.1). In a second step, this climate is applied in cycles but within the HTM framework to simulate progressive degradation of the sandstone (Section 5.2). Note that the identified worst climate case can also be used for accelerated weather testing in experimental settings.

5.1 HT simulations without material degradation

To get started, the moisture field is calculated regardless of material degradation, keeping the hygro-thermal behavior unaltered throughout the simulations. The identification of the most critical case involves minimizing an objective function (Section 5.1.2) that requires a prior parameterization of climatic conditions, as discussed in Section 5.1.1.

5.1.1 Parameter space for climatic conditions

Climatic conditions can be extremely diverse, including relative humidity, wind-driven rain, solar irradiation, temperature, wind velocity, and other factors. This makes it difficult to identify critical conditions and their history that could promote intrinsic material damage or degradation. Only if those are known, lab studies of climate-induced stone degradation, that rely on accelerated weather testing, become feasible [21, 20]. To stay within the operational modes of typical climate-controlled chambers and for simplicity, wetting-drying cycles are investigated with rain for wetting and a high temperature with low relative humidity for drying. Five independent climatic parameters, related to these two processes are chosen: rain flux F_{rain}, raining time t_{rain}, surface temperature of the sandstone during drying T_{dry}, relative humidity for drying RH_{dry}, and drying time t_{dry}. Note that DELPHIN is capable of considering excess water from the rain as runoff, which is realistic [7]. Another noteworthy point is that the material's surface temperature is used as a drying parameter rather than the ambient temperature. This is because the drying process is also influenced by solar irradiation (or infrared heating inside chambers) in addition to ambient temperature. The surface temperature can be regarded as a result of both factors. The temperature and relative humidity during the rain are taken as constant values of 20 °C and 98 % in the simulations. The hygro-thermal boundary conditions of the model are displayed in Fig. 13 together with the climatic parameters. The parametric space with feasible ranges of the above five parameters is given in Table 3.

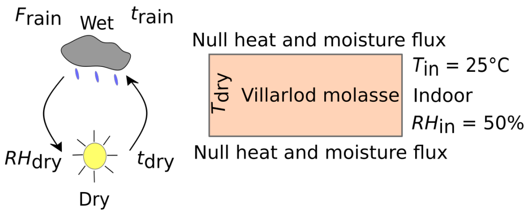

Figure 13: Hygro-thermal boundary conditions of the model (T_{in} and R_{in} for indoor temperature and relative humidity respectively).

5.1.2 Worst climatic conditions

Damage develops as a consequence of residual stress, which can emerge from differential, self-restrained swelling due to hygric or thermal inhomogeneities. Since thermal expansion is neglected and hygric behavior is kept unaltered at this stage of the calculations, the moisture gradient must be considered as the driver of damage. Note that the moisture field will be one-dimensional in this case. As shown in Ref. [20] for Villarlod molasse, at a depth of 6 cm water accumulation and degradation are observed, which eventually develop into contour scaling. For simplicity, the liquid content θ_l is averaged in two sub-zones (0–4 cm and 4–8 cm) to calculate the moisture gradient. A clear picture can be obtained, when looking at θ_l for a sample parameter set of $\{F_{\text{rain}},t_{\text{rain}},T_{\text{dry}},RH_{\text{dry}},t_{\text{dry}}\}=\{0.002\,\text{dm}^3\,\text{m}^{-2}\,\text{s}^{-1},5\,\text{h},35\,°\text{C},30\,\%,48\,\text{h}\}$. In Fig. 14a, $\theta_l(t)$

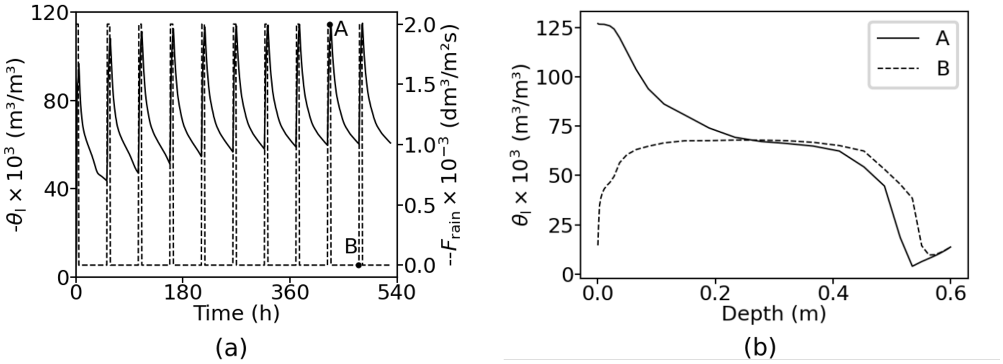

Figure 14: Results for a typical simulation with $F_{\text{rain}} = 0.002\text{L}\,\text{m}^{-2}\,\text{s}^{-1}$, $t_{\text{rain}} = 5\,\text{h}$, $T_{\text{dry}} = 35\,°\text{C}, RH_{\text{dry}} = 30\,\%$, and $t_{\text{dry}} = 48\,\text{h}$: (a) Liquid content θ_l at a depth of 5 cm; (b)Moisture profiles at states A and B.

is given at a depth of 5 cm as a function of time for 10 cycles, after which

θ_l reached a periodic steady state. Two states exhibit extreme values: state A is the moment when wetting finishes in one cycle, while state B is at the end of a cycle after drying. In a typical wetting-drying cycle, these two states (A and B in Fig. 14b) potentially have the highest moisture gradients, and it is sufficient to focus on them. Therefore, the objective function for maximization takes the form

$$f_{\mathrm{obj}}(F_{\mathrm{rain}}, t_{\mathrm{rain}}, T_{\mathrm{dry}}, R_{\mathrm{dry}}, t_{\mathrm{dry}}) = (\theta_{\mathrm{l,A}}^{0-4,\mathrm{avg}} - \theta_{\mathrm{l,A}}^{4-8,\mathrm{avg}}) + (\theta_{\mathrm{l,B}}^{4-8,\mathrm{avg}} - \theta_{\mathrm{l,B}}^{0-4,\mathrm{avg}}), \tag{32}$$

where $\theta_{\mathrm{l},k}^{0-4,\mathrm{avg}}$ and $\theta_{\mathrm{l},k}^{4-8,\mathrm{avg}}$ ($k = A, B$) are average liquid contents of the regions 0–4 cm and 4–8 cm, respectively. The two terms on the right-hand side of Eq. 32 share the same denominator when calculating the moisture gradient, and can therefore be omitted.

The maximum of the objective function Eq. 32 is obtained with a Bayesian optimization algorithm. As a large number of hygro-thermal simulations are required for optimization, a surrogate model is first trained on the hygro-thermal model using a Gaussian Process Regressor (GPR). For training the surrogate model, the Latin Hypercube Sampling technique is adopted with 200 samples from the feasible parameter ranges given in Table 3. Note that for increased performance, the five climatic parameters are normalized to the range $[0, 1]$ prior to training. The comparison between the predictions of the surrogate and original models is shown in Fig. 15, demonstrating good agreement. Finally, the surrogate model is used in the Bayesian optimization scheme to calculate a set of values (see Table 3) that maximize Eq. 32 and, therefore, the damage propagation risk. Note that due to this engineering approach, there is no claim of uniqueness of the value set. Nevertheless, these values result in quite harsh conditions that would be useful and rational conditions for accelerated weather testing of climatic material degradation, and are a good choice for HTM simulations.

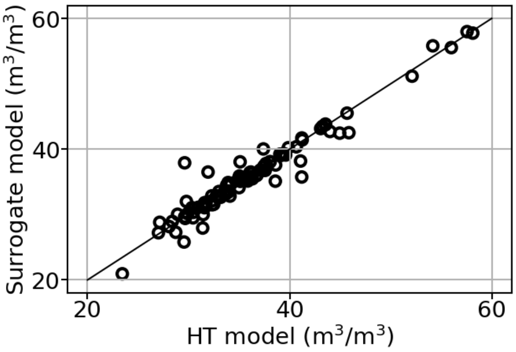

Figure 15: Comparison of predicted θ_l from surrogate and original models.

Table 3: Ranges and critical values of climatic parameters.

Parameter	**Definition**	**Range**	**Critical value**
$F_{\text{rain}}\,(\text{dm}^3\,\text{m}^{-2}\,\text{s}^{-1})$	Rain flux	$[0.0005, 0.002]$	0.0018
$t_{\text{rain}}\,(\text{h})$	Raining time	$[1, 7]$	6
$T_{\text{dry}}\,(^{\circ}\text{C})$	Surface temperature for drying	$[25, 40]$	28.8
$RH_{\text{dry}}\,(\%)$	Relative humidity for drying	$[20, 50]$	43.1
$t_{\text{dry}}\,(\text{h})$	Drying time	$[48, 120]$	66

5.2 HTM simulations with material degradation

Now that all model parameters are identified (Tables 1, 2) and the set of values for the most critical climatic conditions is determined (Table 3), the fully coupled HTM framework can be applied to capture the structural response of a block of Villarlod molasse with climate induced material degradation. For demonstration purposes, a quite high vertical load is applied on the top reference point of the contact surface with 4 MN, which corresponds to 17 % of the compressive strength of Villarlod molasse (40 MPa). To introduce material heterogeneity on the material patches, an initial damage value D_0 is sampled from the interval $[0, 0.04]$. For comparison, only the first 10 cycles are simulated for distinct values β of the damage evolution law Eq. 23, namely $\beta = 5000$ and $\beta = 4000$.

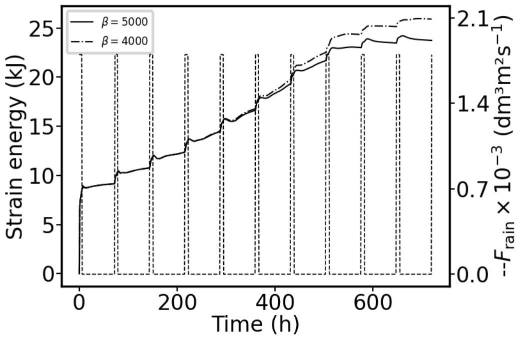

Figure 16: Evolution of strain energy for $\beta = 5000$ and $\beta = 4000$.

The evolution of the total strain energy provides a first global picture of the system behavior. In Fig. 16, the evolutions over the first 10 cycles for the two different values of the damage law are compared. In general, the strain energy increases and converges, analogous to the moisture reaching the periodic steady state. As total moisture increases, Young's modulus E decreases, leading to higher strain energy for a constant load. This is also evident in every moistening phase, by a sharp increase. As damage accumulates, E is further decreased, amplified by the increased moisture content in damaged regions, which further reduces E. In the drying phase of all cycles, one first observes a drop in strain energy as stiffness is restored by drying. In fact, the moisture gradient reverses (see Fig. 14b) and induced stresses can further increase the strain energy during drying. The higher energy for $\beta = 4000$ points at a larger overall damage due to the choice of that parameter.

A deeper insight into the evolution of damage is given by visualizing snapshots of the damage state variable at the end of cycles 2, 4, 6, 8, and 10 in Fig. 17. It is striking to observe that damage does not develop at the surface but first at a depth of 3–5 cm, which is in agreement with onsite contour scaling observations [20]. This is because damage is mainly driven by tensile stress in cohesive frictional materials, and the sandstone surface is free of tensile stress due to vertical compression. Inside the sandstone, however, the material is under a constrained state, and tension can occur. At later stages, damage localizes and progresses, forming shear band configurations under the characteristic 45° angle. In the comparison of the damage parameters, one can see that damage progresses faster for smaller values of β. Note that the model is targeted at dispersed damage in the framework of continuum damage mechanics. This way, one can identify zones of material degradation, where fractures will form. The fracture formation and growth are not part of the model. Due to rather high loads and the limitation of $D \leq 0.4$, one observes large, unrealistic damage regions at later states, as fracture localization is suppressed. Nevertheless, there is indirect evidence that the degraded region must be quite extensive, since multiple ice lenses are observed, which can only form in the degraded Villarlod molasse, as shown by [33].

The moisture profiles of the HT simulation, exemplified in Fig. 14, did not account for the consequences of changes in hygric behavior due to damage. With coupled HTM simulations, however, one can observe significant differences, as shown by comparing the moisture distribution at the end of 10 wetting-drying cycles for the HTM models with the HT model in Fig. 18. It is found that moisture accumulation is closely related to the localization of damage in the sandstone, although their depths differ slightly. Generally, higher moisture content occurs in a more damaged zone that is better able to retain water. The surface region undergoes rapid saturation and drying throughout the wetting-drying cycles, while water at a certain depth is trapped and constrained by the sandstone's moisture-transport properties. Furthermore, water penetration into the deep region is rather slow, resulting in a relatively dry core. The distinct moisture accumulation layer forming at a depth of 6–10 cm is only observed for the HTM models and is consistent with on-site observation from impedance measurements on the Cathedral of Lausanne, as presented in Ref. [20].

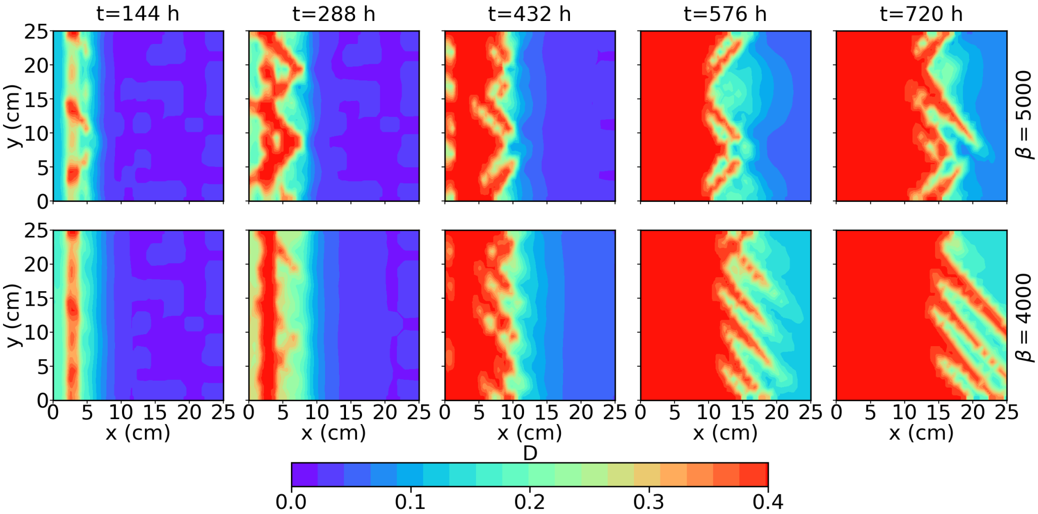

Figure 17: Evolution of damages in the Villarlod molasse block at different times for $\beta = 4000$ (x and y for depth and height of the block, respectively). As the damage evolution is not significant for $x > 25$cm, the images are cropped.

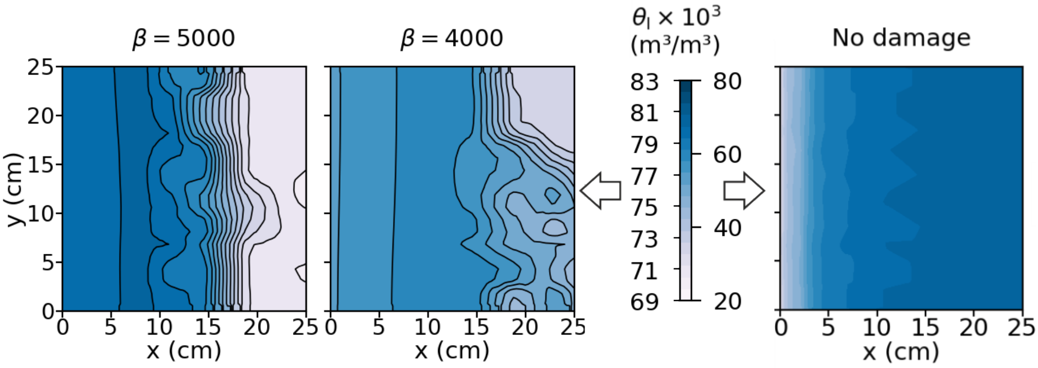

Figure 18: Moisture distribution in the Villarlod molasse block at the end of 10 wetting-drying cycles for $\beta = 5000$ and $\beta = 4000$ and without damage (right).

Damage is driven by residual stress and by stress arising from the compressive loading through the normal contact with the rigid plate on top. Only at the start of the simulation, a uniform pressure of about 7 MPa is present. As moisture fields develop, material expands or shrinks, and compliances change due to moisture or possible damage progression, pressure distributions quickly become complicated. Fig. 19 shows the time evolution of the contact pressure distribution on the top of the block for the two distinct damage parameters β, as well as with suppressed damage evolution. With the wetting and drying of the sandstone, significant redistribution of pressure occurs due to several competing factors: In the wetting phases, hygric expansion increases pressure in swelling parts, which, at the same time, require less stress for deformation, as compliance and maybe even damage increase. The emerging pattern across all three cases is that the stone in the deep region, which is less damaged and moist, plays a major role in load carrying. The role of damage is clearly seen when comparing the different cases, including the suppressed damage case $D = 0$. It is interesting to note that different β values do not cause a significant difference in the pressure distribution. For $D = 0$, however, the exterior regions of the stone can indeed take excess load in the wetting phase towards the periodic steady state, but interestingly, with a maximum in the depth, where scaling damage is observed to develop.

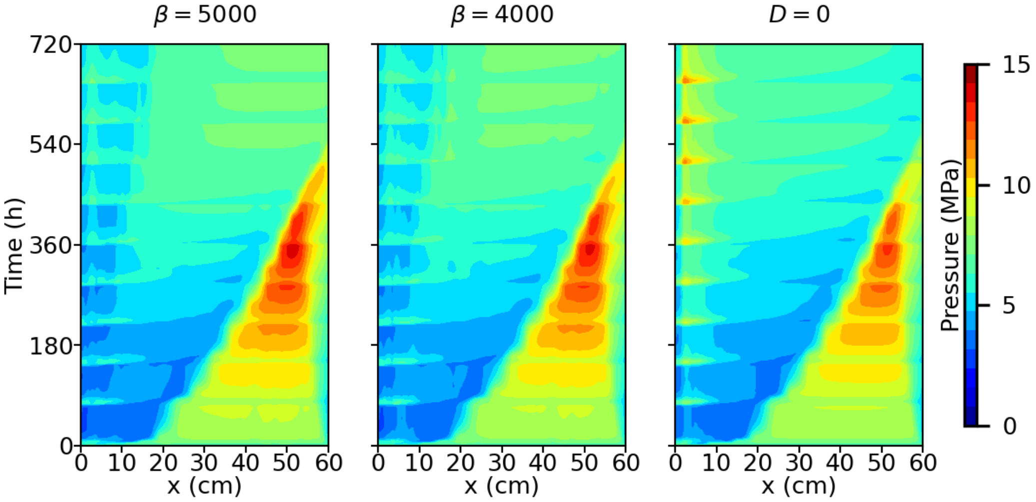

Figure 19: Pressure on the top of the Villarlod molasse block for $\beta = 5000$, $\beta = 4000$, and $D = 0$.

If the material regions of the exterior surface are most affected by moisture changes, reducing pressure by introducing recessed horizontal joints could help prevent contour scaling. To clarify this question, the damage states after two cycles for different recess depths of 5 cm and 10 cm are compared in Fig. 20. As shown, the damage pattern is markedly different, localized at the edge of the rounded contact surface. In addition, for increasing recess depth, damage evolves more slowly. This is due to a higher moisture gradient at 5 cm than at 10 cm depth, and thus the higher residual stress in the structure superimposes on the stress state caused by the compression, in addition to a higher overall moisture content that lowers strength. The damage localization is explained by the contact pressure (see Fig. 21), which shows clear peaks at the position of load introduction. Even though their magnitudes might be too high due to artifacts arising from the contact calculation, one should still expect the failure origin in those regions. Note that after two cycles, the periodic steady state has not yet been reached, as evident from the height-averaged moisture profiles.

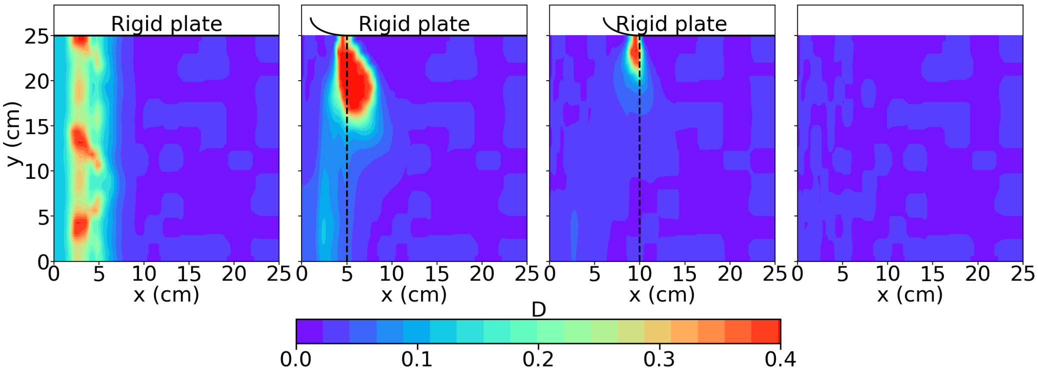

Figure 20: Damage fields ($\beta = 5000$) at $t = 144\,\mathrm{h}$ for no pressure and different recess depths (0, 5 cm, and 10 cm) under the same vertical load and no load at all (right).

Interestingly, if no external load is applied (see Fig. 20 right), residual stresses alone do not suffice to drive damage. This is an important finding, showing that accelerated weather testing in climate rooms can trigger contour scaling only when samples experience both climatic and external loading simultaneously.

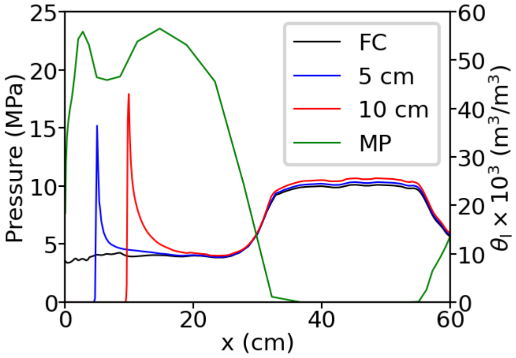

Figure 21: Pressure distributions on the top of the Villarlod molasse block under the same vertical load at $t = 144\,\mathrm{h}$ for different recess depths and moisture profile for the fully covered case. ($\beta = 5000$, FC: fully covered, MP: moisture profile).

6 Conclusions

This study investigated the coupling between moisture evolution and material degradation in clay-bearing sandstone under wetting-drying cycles. Pure HT simulations are first conducted to identify the worst climatic conditions to be applied in a fully coupled HTM framework with damage evolution for a block simultaneously loaded by a vertical force. The damage localization and moisture accumulation in the sandstone block are found to be closely related. They match on-site observations and measurements at the Cathedral of Lausanne. It is further shown that the pressure distribution at the top of the sandstone also significantly affects the damage pattern. The major conclusions of this study are as follows:

- Contour scaling in the clay-bearing sandstone can emerge solely as a result of moisture cycling without degradation by freezing or salt crystallization. Hence, it is no wonder that contour scaling is also observed in places without freezing or salt problems, e.g., the temple of Angkor Wat in Cambodia. Nevertheless, freezing and salt crystallization are potential damage mechanisms that can accelerate damage propagation and deterioration.

- The initial damage localization zone after several moisture cycles has a similar depth as on-site observation of contour scaling at Cathedral of Lausanne, i.e., 3–5 cm as presented in Ref. [20].

- Moisture accumulates at a depth of 6–10 cm as a consequence of damage-induced changes of hygric properties. It agrees well with impedance measurements at Cathedral of Lausanne shown in Ref. [20].

- Damage localizes at a depth of several centimeters in the sandstone when the whole top surface is carrying the load, whereas it initiates directly from the edge of the contact surface when the sandstone block is partially loaded due to recessed horizontal joints. Wide zones of material degradation emerge, which are the condition for ice lensing, as shown in Ref. [33].

Although the fully coupled HTM framework can capture the damage and water accumulation phenomena observed on site, the mechanical model presented in this paper remains subject to several assumptions. These include damage evolution laws under different moisture states, the decay of Young's modulus with moisture content, and many others, which call for further experimental studies of hygro-mechanical behavior. Many insights into the behavior can only be obtained through expensive experimental setups, e.g., *in situ* neutron tomography. Grain-scale simulations using Discrete Element Methods (DEM) with models of quartz grains bonded by calcite and swelling clay, whose properties change with moisture content, could yield a greater understanding of hygro-mechanical behavior. Under freezing conditions, ice in macropores that influences mechanical behavior can also be modeled using particles in DEM. The constitutive behavior could be elaborated using a micro-mechanical grain-scale model under variable moisture content and temperature conditions. This could be integrated into a continuum solver for the structural response of clay-bearing sandstone under changing climatic conditions. Works in this direction are in progress.

Nomenclature

$*_\mathrm{E}$	Fitting parameters for the function of Young's modulus with respect to moisture content ($* = A, B, C$)
$*_\epsilon$	Fitting parameters for the hygric expansion curve ($* = A, B, C, D, F$)
$*_{\sigma_\mathrm{t}}$	Fitting parameters for the function of tensile strength with respect to moisture content ($* = A, B, C$)
α, s	Parameters of the moisture storage function
β	Damage parameter in the damage evolution law
$\boldsymbol{\epsilon}_*$	Hygric, elastic, and total strain ($* = \mathrm{hyg}, \mathrm{ela}, \mathrm{tot}$)
$\boldsymbol{S}_0$	Undamaged secant stiffness matrix
$\dot{m}_k^*$	Moisture flux density ($k = \mathrm{tot}, \mathrm{v}, \mathrm{l}; * = \mathrm{par}, \mathrm{ser}$)($\mathrm{kg\,m^{-2}\,s^{-1}}$)
$\epsilon_\cdot$	Maximum principal strain and failure strain ($\cdot = max, f$)
η	Viscosity parameter for viscous damage variable
η_l	Dynamic viscosity of liquid water ($\mathrm{Pa\,s}$)
λ	Thermal conductivity ($\mathrm{W\,m^{-1}\,K^{-1}}$)
λ_dry	Thermal conductivity of dry sandstone($\mathrm{W\,m^{-1}\,K^{-1}}$)
$\lambda_\mathrm{l}, \mu_\mathrm{l}$	Lamé constants (Pa)
μ_dry	Vapor resistance from the dry cup test
ν	Poisson's ratio
ρ_*	Mass density of liquid water, vapor, or dry air ($\mathrm{kg\,m^{-3}}$) ($* = \mathrm{w}, \mathrm{v}, \mathrm{a}$)
σ_lg	Surface tension at the liquid-air interface ($\mathrm{N\,m^{-1}}$)
σ_t	Tensile strength (Pa)

θ_*	Volumetric fraction of liquid or gaseous phase ($\mathrm{m^3\,m^{-3}}$) ($* = \mathrm{l}, \mathrm{g}$)
θ_{por}	Porosity
$\theta_\cdot$	Capillary saturation, transition moisture content, and effective saturation ($\cdot = \mathrm{cap}, \mathrm{trans}, \mathrm{eff}$) ($\mathrm{m^3\,m^{-3}}$)
φ	Relative humidity
A_{l}	Parameter of the liquid conductivity function ($\mathrm{kg\,N\,m^{-3}\,s^{-1}}$)
D	Scalar damage variable
D_{vis}	Viscous damage variable
D_{v}	Vapor diffusion coefficient ($\mathrm{m^2\,s^{-1}}$)
E	Young's modulus (Pa)
E_0	Young's modulus of intact Villarlod molasse (Pa)
F_{rain}	Rain flux ($\mathrm{dm^3\,m^{-2}\,s^{-1}}$)
g_k	Gravitational acceleration component for direction k ($\mathrm{m\,s^{-2}}$)
h_*	Enthalpy ($* = v, a$) (J)
h_c	Size of elements in contact with the rigid plate (m)
$j^*_{k,\mathrm{diff}}$	Heat flux via conduction ($\mathrm{J\,m^{-2}\,s^{-1}}$) and the moisture flux ($\mathrm{kg\,m^{-2}\,s^{-1}}$) in dimension k ($* = Q, m_v$)
K_*	Liquid or vapor conductivity (s) ($* = l, v$)
$K_{\mathrm{l}}(*)$	Liquid conductivity at capillary and effective saturation ($* = \theta_{\mathrm{cap}}, \theta_{\mathrm{eff}}$) (s)
K_{ct}	Contact stiffness between the sandstone and the rigid plate on the top of the block ($\mathrm{GPa\,m^{-1}}$)
p_*	Capillary and vapor pressure ($* = \mathrm{c}, \mathrm{v}$) (Pa)
p_{clog}	Logarithmic capillary pressure (log Pa)
p_{p}	Proportion of parallel moisture transport in serial-parallel model
$p_{\mathrm{v,sat}}$	Saturation vapor pressure (Pa)
r	Pore radius (m)
R_{v}	Ideal gas constant of vapor ($\mathrm{J\,kg^{-1}\,K^{-1}}$)
RH_*	Relative humidity during drying and indoor relative humidity ($* = \mathrm{dry}, \mathrm{in}$) (%)
T_*	Surface temperature during drying and indoor temperature ($* = \mathrm{dry}, \mathrm{in}$) (°C)

t_* Drying and raining time ($* = \text{dry}, \text{rain}$) (h)

u Energy density ($\mathrm{J\,m^{-3}}$)

v Phase velocity ($\mathrm{m\,s^{-1}}$)

7 Acknowledgement

This work is financially supported by the ETH-grant (ETH-C-01 22-1) "Protecting Sandstone Monuments". The authors acknowledge Asel Maria Aguilar Sanchez for SEM images, Camilla Tennenini and Anjo Weichbrodt for help with the experiments, Timmothy Wangler, Robert Flatt, and David Kammer for constructive discussions, and the Delphin developers for ongoing support with the software.

8 Declaration of generative AI and AI-assisted technologies in the manuscript preparation process

During the preparation of this work, the authors used Grammarly for language corrections. After using this tool/service, the authors reviewed and edited the content as needed and take full responsibility for the content of the published article.

References

[1] Benavente, D., Cultrone, G., and Gómez-Heras, M. (2008). The combined influence of mineralogical, hygric and thermal properties on the durability of porous building stones. *European Journal of Mineralogy* 20 (4): 673–685.

[2] Burdine, N. (1953). Relative permeability calculations from pore size distribution data. *Journal of Petroleum Technology* 5 (03): 71–78.

[3] Delgado Rodrigues, J. (2001). Consolidation of decayed stones. a delicate problem with few practical solutions. In *International Seminar on Historical Constructions*, Pp. 3–4. Guimarães Guimaráes.

[4] Demoulin, T. (2016). *Durability of clay-bearing sandstone and its repair by viscoelastic mortars*. PhD thesis. ETH Zurich.

[5] Dullien, F. A. (2012). *Porous media: fluid transport and pore structure.* Academic press, San Diego, CA.

[6] Elert, K., Ruiz-Agudo, E., Jroundi, F., Gonzalez-Muñoz, M. T., Fash, B. W., Fash, W. L., Valentin, N., de Tagle, A., and Rodriguez-Navarro, C. (2021). Degradation of ancient Maya carved tuff stone at Copan and its bacterial bioconservation. *NPJ Materials Degradation* 5 (1): 44.

[7] GmbH, B. D. S. (2025). Delphin (6.1.7).

[8] Grunewald, J. (1997). *Diffusiver und konvektiver Stoff-und Energietransport in kapillarporösen Baustoffen.* PhD thesis. TU Dresden.

[9] Grunewald, J. and Häupl, P. (2002). Ein Modell zur Beschreibung der feuchteabhängigen Dampfleitfähigkeit kapillarporöser Materialien, 11. In *Symposium on Building Climatology.* TU Dresden.

[10] Hendrickx, R. and De Clercq, H. (2018). Heat and moisture simulations of repair mortars: benchmark experiments and practical cases in conservation. In *Historic Mortars: Advances in Research and Practical Conservation*, Pp. 319–336. Springer.

[11] Jiménez-González, I., Rodríguez-Navarro, C., and Scherer, G. W. (2008). Role of clay minerals in the physicomechanical deterioration of sandstone. *Journal of Geophysical Research: Earth Surface* 113 (F2): 1–17.

[12] Leisen, H. (2002). Contour scaling: the disfiguring disease of Angkor Wat reliefs. *Museum International* 54 (1-2): 85–92.

[13] Li, S., Yang, Z., Gao, Y., Liu, X., and Jin, X. (2024). The effect of clay swelling on crack generation in red stratum soft rock during water-induced disintegration: a matrix-based discrete element simulation study. *Bulletin of Engineering Geology and the Environment* 83 (12): 489.

[14] Li, Y., Xie, H., Feng, G., Zhang, R., Zhang, G., Xu, Z., Feng, T., Wang, D., Yi, X., Chen, M., et al. (2022). Experimental study on the failure characteristics and damage evolution of sandstones from typical buried depths in high in situ stress area. *Lithosphere* 2022 (Special 10).

[15] Linde, P., Pleitner, J., de Boer, H., and Carmone, C. (2004). Modelling and simulation of fibre metal laminates. In *ABAQUS Users' conference*, volume 421.

[16] Liu, K., Sheng, J. J., and Zhang, Z. (2020). A simulation study of the effect of clay swelling on fracture generation and porosity change in shales under stress anisotropy. *Engineering Geology* 278: 105829.

[17] Murakami, S. (2012). *Continuum damage mechanics: a continuum mechanics approach to the analysis of damage and fracture*, volume 185. Springer Science & Business Media, Nagoya, Japan.

[18] Nicolai, A. (2008). *Modeling and numerical simulation of salt transport and phase transitions in unsaturated porous building materials.* Syracuse University, Syracuse University, USA.

[19] Peng, X. and Horn, R. (2005). Modeling soil shrinkage curve across a wide range of soil types. *Soil Science Society of America Journal* 69 (3): 584–592.

[20] Praticò, Y. (2020). *Practical applications of science for the conservation of built heritage: Strategies based on the analysis of rare events.* PhD thesis. ETH Zurich.

[21] Praticò, Y., Girardet, F., and Flatt, R. (2016). Strategies for the conservation of built heritage based on the analysis of rare events. *Science and Art: A Future for Stone.*

[22] Qi, W., Wang, C., Zhang, Z., Huang, M., and Xu, J. (2022). Experimental investigation on the impact of drying–wetting cycles on the shrink–swell behavior of clay loam in farmland. *Agriculture* 12 (2): 245.

[23] Ruedrich, J., Bartelsen, T., Dohrmann, R., and Siegesmund, S. (2011). Moisture expansion as a deterioration factor for sandstone used in buildings. *Environmental Earth Sciences* 63: 1545–1564.

[24] Scheffler, G. A. (2008). *Validation of hygrothermal material modelling under consideration of the hysteresis of moisture storage.* PhD thesis. Dresden University of Technology.

[25] Siegesmund, S., Gross, C. J., Dohrmann, R., Marler, B., Ufer, K., and Koch, T. (2023). Moisture expansion of tuff stones and sandstones. *Environmental Earth Sciences* 82 (6): 146.

[26] Stück, H. L. (2013). *Dimensional Sandstones: Weathering Phenomena, Technical Properties and Numerical Modeling of Water Migration.* PhD thesis. Niedersächsische Staats-und Universitätsbibliothek Göttingen.

[27] Sun, X., Shi, F., Luan, Z., Yang, L., Ding, J., He, L., and Zhang, Y. (2023). Constitutive model and microscopic mechanism for sandstone strength softening damage. *Rock Mechanics and Rock Engineering* 56 (1): 797–813.

[28] Tiennot, M., Bourgès, A., and Mertz, J. (2016). Influence of the Villarlod molasse anisotropy on cracking advances in the comprehension of the desquamation mechanisms. In *Science and Art: A Future for Stone*, Pp. 155–163. University of the West of Scotland.

[29] Tiennot, M., Mertz, J.-D., and Bourgès, A. (2019). Influence of clay minerals nature on the hydromechanical and fracture behaviour of stones. *Rock Mechanics and Rock Engineering* 52: 1599–1611.

[30] Veniale, F., Setti, M., Rodriguez-Navarro, C., and Lodola, S. (2001). Role of clay constituents in stone decay processes. *Materiales de construcción* 51 (263-264): 163–182.

[31] Vogelsang, S., Fechner, H., and Nicolai, A. (2013). *Delphin 6 Material File Specification: Version 6.0.* Sächsische Landesbibliothek-Staats-und Universitätsbibliothek Dresden, Dresden, Germany.

[32] Wang, T. and Yan, C. (2023). Investigating the influence of water on swelling deformation and mechanical behavior of mudstone considering water softening effect. *Engineering Geology* 318: 107102.

[33] Wang, Y. and Wittel, F. K. (2025). Ice lensing in sandstone walls under monotonic and cyclic climatic conditions. *International Journal of Heat and Mass Transfer* 238: 126473.

[34] Wangler, T. (2016). Swelling clay and its inhibition in the Villarlod molasse. In *Science and Art: A Future for Stone*, Pp. 189–196. University of the West of Scotland.

[35] Wangler, T. (2023). Mechanism of clay swelling in Villarlod molasse: a Swiss sandstone. *Environmental Earth Sciences* 82 (11): 259.

[36] Wangler, T. and Scherer, G. W. (2008). Clay swelling mechanism in clay-bearing sandstones. *Environmental Geology* 56 (3): 529–534.

[37] Wangler, T. P., Stratulat, A., Duffus, P., Prévost, J. H., and Scherer, G. W. (2011). Flaw propagation and buckling in clay-bearing sandstones. *Environmental earth sciences* 63: 1565–1572.

[38] Wu, Y., Wang, H., Zhang, Y., Lyu, C., Liu, Y., and Wang, W. (2025). Deterioration mechanism and statistical damage constitutive model of red-bed soft rock with different moisture content. *Pure and Applied Geophysics* 182: 189–208.

[39] Zehnder, K. (1984). Weathering of molasse sandstones on monuments and natural outcrops. *Beiträge zur Geologie der Schweiz. Kleinere Mitteilungen.*

[40] Zhang, Z., Cui, W., Liu, Z., Liu, W., Xi, B., and Chen, M. (2023). Study on the cracking mechanism of strongly weathered purple mudstone under wetting and drying effect through experiments and molecular dynamics simulation. *Construction and Building Materials* 403: 133104.

[41] Zhao, J. and Plagge, R. (2015). Characterization of hygrothermal properties of sandstones—impact of anisotropy on their thermal and moisture behaviors. *Energy and Buildings* 107: 479–494.